Trends in Analytical Chemistry 172 (2024) 117588

Contents lists available at ScienceDirect

Trends in Analytical Chemistry

journal homepage: www.elsevier.com/locate/trac

Lung disease characterised via synchrotron radiation micro-CT and digital volume correlation (DVC)

Hari Arora [a,*], Dale Kernot [a], Louis Giron [a], David Howells [a], Michael Darcy [a], Makoto Hoshino [b], Kentaro Uesugi [b], Raoul van Loon [a], Gaku Tanaka [c], Toshihiro Sera [d]

[a] Biomedical Engineering Simulation and Testing Lab, Department of Biomedical Engineering, Swansea University, UK
[b] SPring-8, Japan
[c] Department of Mechanical Engineering, Chiba University, Japan
[d] Department of Medical and Robotic Engineering Design, Tokyo University of Science, Japan

ARTICLE INFO

Keywords:
Lung mechanics
Synchrotron
Tomography
Digital volume correlation (DVC)

ABSTRACT

The study of lung mechanics is important to futureproof resilience against potential novel threats to lung health. Medical imaging provides insight to lung function. High-resolution, high-speed synchrotron radiation micro-CT imaging at SPring-8 (Japan) and *in situ* mechanics were used to characterize healthy and diseased airways. Synchrotron radiation was important to maximize speed and spatial resolution to map the lung architecture clearly. Links between global lung mechanical measurements (pressure-volume) and regional tissue strains were made. Tissue strains were computed from a sequence of tomograms during a respiratory cycle, demonstrating clear differences for the surfactant-free lungs compared to the controls. Poorly ventilated areas were identified within three-dimensional strain maps computed via digital volume correlation. Occluded pathways at low pressures were seen to be opened at higher pressures, augmenting the deformation pathways. The results will aid correlations between microscale and macroscale measurements and the potential impact on patient management guidelines for mechanical ventilation.

1. Intro

Improving the sensitivity of lung health diagnostics is crucial, given many people suffer from undiagnosed respiratory illnesses, which remains a major cause of death worldwide. In the UK, 10,000 people are diagnosed each week and approximately one in five people develop asthma, COPD or other long-term respiratory illnesses [1]. Globally, specific diseases such as asthma and COPD resulted in almost 4 million deaths in 2019 [2]. Understanding distinct alterations in lung mechanical behaviour for various diseases presents an opportunity to improve quality-adjusted life years through more prompt and accurate diagnosis.

Environmental factors (e.g. exposure to pollutants/toxins), illness (e.g. pneumonia/COVID-19) and social habits (e.g. smoking) compound the degradative effects seen in the population's lung health. Therefore, higher resolution solutions that map the biomechanical impact of a given disease mechanism will help bridge the gaps in knowledge, which were further revealed in the spotlight of the recent pandemic. There remains a distinct need to study fundamental lung mechanical alterations on a local scale to comprehend their impact on global, organ-level performance. This study focuses on the impact caused by alterations to the airway fluid lining on the added mechanical tissue burden experienced during mechanical ventilation.

Surfactant is a complex mixture of lipids and proteins that lines the inner surface of the lungs. Its primary role is to reduce surface tension within the alveoli, preventing collapse during exhalation and promoting ease of airway opening (increasing lung compliance). Surfactant deficiency can be observed in premature infants as well as other respiratory disorders in adults. In very unwell patients in intensive care, invasive mechanical ventilation may be performed, which has multiple side effects including amongst others, alteration to fluid balance in the airways and overdistension of delicate airways. Advanced clinical imaging methods can visualize changes in lung structure and mechanics. Improvements in magnetic resonance imaging (MRI) technology, for instance, have led to enhanced temporal resolution, allowing researchers to capture dynamic processes. However, clinical imaging still cannot provide detailed information linking the microscale to the macroscale mechanics nor capture the dynamics in the smallest airways during respiration.

* Corresponding author.
E-mail address: hari.arora@swansea.ac.uk (H. Arora).

https://doi.org/10.1016/j.trac.2024.117588
Received 30 October 2023; Received in revised form 27 January 2024; Accepted 5 February 2024
Available online 7 February 2024

Advances in micro-CT technology have facilitated high-resolution imaging of lung structures, enabling the visualization with exceptional detail [3–12]. Synchrotron micro-CT enables improved phase contrast with no need for complex sample preparation, which lends itself ideally towards imaging and providing a wide range of quantitative measurements [13–15]. Various biomaterials have been explored including both hard [16–24] and soft tissues [3–7,10–12,25–28]. Quantitative analysis of airway dynamics and alveolar mechanics has been demonstrated [4,5,28–31] including *in vivo* [3,6,12,27,32]. Synchrotron micro-CT is continuously evolving across beamlines, which can provide exceptionally high-resolution images to the sub-micron level [33]. Best practice and guidelines on how to perform *in situ* mechanics are also continually being reported within the wider biomaterials community [34].

Synchrotron micro-CT imaging of the lung enables detailed visualizations down to the alveolar level. This project focuses on the links between local tissue strains and the impact on global mechanical measures. Other classic histological methods can highlight structural and functional changes in lung tissue. Discerning between disease or injury types, the pathology severity, as well as therapeutic efficacy can be achieved through histological studies [35–39]. These methods require fixed samples and are destructive. However, the advancements of synchrotron micro-CT have enabled comparable spatial resolution of imaging to be achieved in non-fixed samples [5]. Beam properties, optics and the targeted field of view dictate the spatial resolution. Whilst the viscoelastic, or time-dependent, nature of target materials needs to be understood and imaging speed optimised to mitigate motion blur in non-fixed samples.

The unique capabilities of synchrotron sources enable dynamic imaging with high temporal resolution, capturing physiologically relevant information about breathing dynamics, airflow patterns, and lung mechanics in health [31,40,41] and disease/injury [5,42–44]. The use of digital volume correlation (DVC) in combination with high-resolution imaging and *in situ* mechanics can be used to quantify the mechanical behaviour of various materials and structures [45–49]. DVC measurements will be advanced to capture biomechanical changes observed in diseased lungs monitored using high-speed synchrotron radiation based micro-CT.

Biomaterials, in particular soft tissues like the lung, exhibit time-dependent behaviour. Therefore, the use of synchrotron radiation at SPring-8, Japan, was important to maximize imaging speed, and spatial resolution, to capture the whole lung architecture [50]. The study of lung mechanics to improve the understanding of disease is important to futureproof resilience against potential novel threats to lung health. In this work, the disease model involved a surfactant-free lung. Although an idealised model of surfactant deficiency is used, it will provide insight to cases where fluid balance adaptations are expected, which alter the fluid lining composition of the airways (e.g. due to oedema). The results obtained from this experiment will be of fundamental significance for correlating relationships between microscale and macroscale measurements of lung function. The potential to impact patient management guidelines for mechanical ventilation is significant, highlighting how much harder the tissue is worked during each cycle.

2. Materials and experimental methods

2.1. Ethics

All experimental protocols were approved (2019A1310) by the SPring-8 (Saitama, Japan) Experimental Animals Care and Use Committee.

2.2. Sample preparation

Intact lungs of six healthy male A/J mice (9 wk, 27.0 ± 1.8 g) were examined. After the mice were euthanized with overdose of anaesthetic, a tracheotomy was performed via a midline incision on the throat and a custom catheter was inserted. The catheter was fastened using a suture, and the junction was fixed in place using cyanoacrylate instant adhesive to prevent any air leaks. This procedure ensured that the thoracic cavity was still intact and closed providing physiologically relevant boundary conditions during mechanical ventilation.

The lung was connected via the tracheal catheter to a custom-made mechanical ventilator device, called a Controlled inflation Tester (CiT) [31]. The global lung pressure-volume relationship was measured and recorded during mechanical ventilation. The lung airway pressure was monitored throughout the experiment. The samples were cycled between 0 cmH_2O and 30 cmH_2O to prevent small airway/alveolar collapse and to evaluate lung compliance prior to and after imaging. The lungs underwent at least 10 cycles of ventilation until the compliance stabilized, indicated by the residual error between cycles dropping below 1%. During ventilation, any collapsed airways reopen and the inactive tissue adapts to movement again, substantially changing the compliance initially. The pressure-volume (P–V) relationship was monitored throughout the test and the characteristic hysteresis loop formed during inflation/deflation was recorded. Note that compliance corrections for the connections between the lung and ventilator were made. As a secondary check on the volume delivered to the lung during each test, the raw images were analysed to quantify the relative volume change via image segmentation. The segmented volume was used to confirm the volume measurements recorded by CiT. These P–V loops are of clinical significance as abnormalities in the curves can be representative of respiratory issues. They are also of interest to engineers as mechanical (primarily elastic) properties of the lung parenchyma can be determined from such curves.

Ventilation prior to imaging ensured all samples had the same baseline mechanical performance and to check that any degradative effects due to time postmortem or beam induced damage were captured. These risks alongside imaging settings have previously been explored [31] and mitigated for within this study. Before imaging, 2–3 cycles were performed and stopped at a set pressure, either 0, 10, 20 or 30 cmH_2O on the inflation phase or deflation phase of a cycle. After a 30s delay to allow air reorganization and a degree of tissue relaxation, a tomogram was acquired. This delay minimized risk of motion blur. The target and actual pressures during imaging were recorded to capture the true loading state. Pressures continued to be recorded during imaging to provide context on the mechanical conditions. All studies here involved eight iterations of ventilation and imaging to occur from the moment of euthanasia. The total time from start to finish was recorded in the range of 33.5–35 minutes for all samples.

One parameter of interest is the compliance of the curve, defined as change in volume divided by change in pressure (the gradient). There are several methods for calculating compliance of a P–V loop but it should be noted that the compliance will vary throughout the curve due to the nonlinear viscoelastic nature of lung tissue. The chord compliance was calculated using two specific volumes assuming a linear P–V relationship. The volume at a cycle's maximum and minimum pressure were used to calculate the compliance. Any regional overdistension of alveoli at high pressures can typically artificially reduce the compliance. Here, regional tissue strains are quantified to enable oversight of such local variations during the quasistatic ventilation procedure. Equally alterations to the fluid lining via alveolar lavage will act to increase surface tension and also lower compliance. Alveolar lavage was performed on three test samples (labelled T1-3) and compared to the three control samples (C1-3).

2.3. Imaging procedure

Tomography was performed at the Biomedical Imaging Beamline BL20B2 [50] of the SPring-8 synchrotron (Japan). Radiation from the bending magnet source is monochromatized and the beam tuned to 25 keV. Test samples were mounted in the beamline, suspended vertically, connected to the controlled inflation tester (CiT) [31]. The sample

support was mounted on orthogonal Sigma Koki crossed roller bearing linear stages [Sigma Koki Co., Ltd., Tokyo, Japan] on top of a Kohzu Precision rotation stage [Kohzu Precision Co., Ltd., Kawasaki, Japan]. An overview of this setup is shown in Fig. 1. Various sample-detector distances were evaluated, with 150 mm chosen to provide adequate phase contrast. Projections were acquired over 180° of continuous rotation at equally spaced 0.2° angular increments.

A high-resolution detector (AA60, Hamamatsu Photonics) was used with a CMOS camera (ORCA-flash 4.0, Hamamatsu Photonics) which has 2048 x 2048 pixels (each pixel is 6.5 μm x 6.5 μm). The focal lengths of the lens were 105 mm in the X-ray detector and 85 mm with the camera. This resulted in an effective pixel size of 8.0 μm x 8.0 μm and the field of view of 25 mm × 25 mm on the phosphor. The phosphor in the X-ray detector was 15 micron-thick P43 (Gd2O2S:Tb). Prior work indicated scan times under 30 s were needed for stability [5,31]. A 25 ms exposure time gave 22.5 s scans, capturing features without motion blur. Before each scan, specimens were cycled on CiT then held at the desired pressure. This ventilation, stabilization, and imaging was repeated to capture deformed geometries along the P–V curve.

2.4. Image preprocessing

Firstly, a segmentation mask needed to be created to remove any background information and regions of the scan that were not relating to the lung tissue of interest. Images were loaded into Matlab and downsized for ease of manipulation to generate a mask. These images were processed to filter out the hard tissue (rib cage) before undergoing texture analysis for segmentation of the lung tissue from the surrounding soft tissues. After this, a manual check is initiated through an interface to inspect and adjust any unsatisfactory slices. Once complete this mask was resized to its original size and overlayed onto the original raw image data. Each stack of segmented images were then saved in a 16-bit *.raww format ready for DVC analysis.

2.5. Digital volume correlation (DVC)

DVC analysis was carried out using DaVis v10.2.1, LaVision, Germany. For each sample, a series of images were processed in DaVis to compute the incremental strain profile from one level of airway pressure to the next. Full-field 3D strains for each lung sample were computed, with sub-volume sizes limited to 32 voxels to generate each strain vector. Each strain stage computed for a given image pair corresponds to a point on the P–V loading curve. Due to potential slight movements of the sample during total test duration (from first scan to last), rigid body motion may have occurred. DaVis software was employed to eliminate any detected rigid body motion before strain computation.

Zero-strain tests were performed to gauge the baseline uncertainty in the strain measurements. Strains from repeat scans obtained at 0 cm H_2O were calculated. As the lung, situated on the stage, interacts with its own weight, elasticity, and its support, the zero-strain test serves as a means to gauge confidence in the strain measurements obtained during the loading cycles. Prior research [31] in highly deformable lung samples revealed strains <5% throughout the volume for this zero-strain test and served as a benchmark here.

3. Results

Images were acquired of the entire lung volume for each sample. Raw images from each control (C) and test (T) sample are shown in Fig. 2. The segmentations are shown side by side with the raw data to illustrate that the segmentation phase did not influence the appearance of the lung itself prior to subsequent strain analysis. There is a distinct difference in appearance between the control samples and those that underwent alveolar lavage. The increased surface tension, arising due to washing away of airway surfactant, has constricted the airways in samples T1-3. All samples were ventilated and scanned at set target pressures. Therefore, it is understandable that the airways of T1-3 would narrow for the same equivalent pressure (due to the elevated surface tension effect). In all samples the respiratory airways are visible.

The integrity of the lungs after exposure to each round of radiation was characterised. Each sample had an established converged compliance reference value prior to the start of each scan. The P–V curve in Fig. 3 illustrates the repeated cycling performed prior to each image being recorded. The classical sigmoidal form of the curve is observed. P–V measurements were monitored prior to each scan to assess any stiffening or damage sustained by the sample either due to degradation (given that these are cadaveric samples) or due to beam damage (radiation/heating). Past work demonstrated that rat lungs could sustain up to 20 exposures prior to degradation becoming significant [31]. All samples here were exposed to eight doses and the repeatability of each P–V curve and stability of compliance illustrates that there is not expected to be any beam damage present. Therefore, all subsequent strain analysis and interpretation of results can focus on lung mechanical phenomena.

To check the volume of air delivered to each lung was as recorded by the ventilator, a secondary assessment of lung volume was performed through segmentation and analysis of the raw lung images. The segmentations for each point on the loading cycle were analysed to quantify the change in volume from the reference zero state to each loading point thereafter. The central plot in Fig. 3 shows the volume extracted from image segmentation for the pressure reading at the point of imaging. There is a reasonable correlation between this secondary volume check and the continuous recordings of the P–V relationship. The final plot shown in Fig. 3 presents the range of P–V curves recorded throughout the experiment, with the range illustrated as the shadow, alongside the first and last recording. This format of curve is then used in subsequent figures for all samples.

Fig. 4 shows raw images for each loading stage for each sample alongside the P–V curves. The raw images confirm that the integrity of each lung sample was maintained from the start to the end of test. The

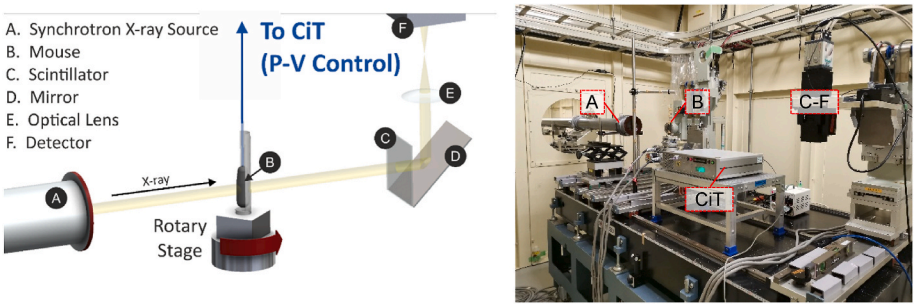

Fig. 1. Overview of experimental setup including a schematic diagram (left) and a photograph of the imaging arrangement taken within the BL20B2 beamline hutch (right). The intact specimen is connected to a mechanical ventilation device, CiT [31], to enable various P–V states to be imaged and for continuous monitoring during the entirety of each test.

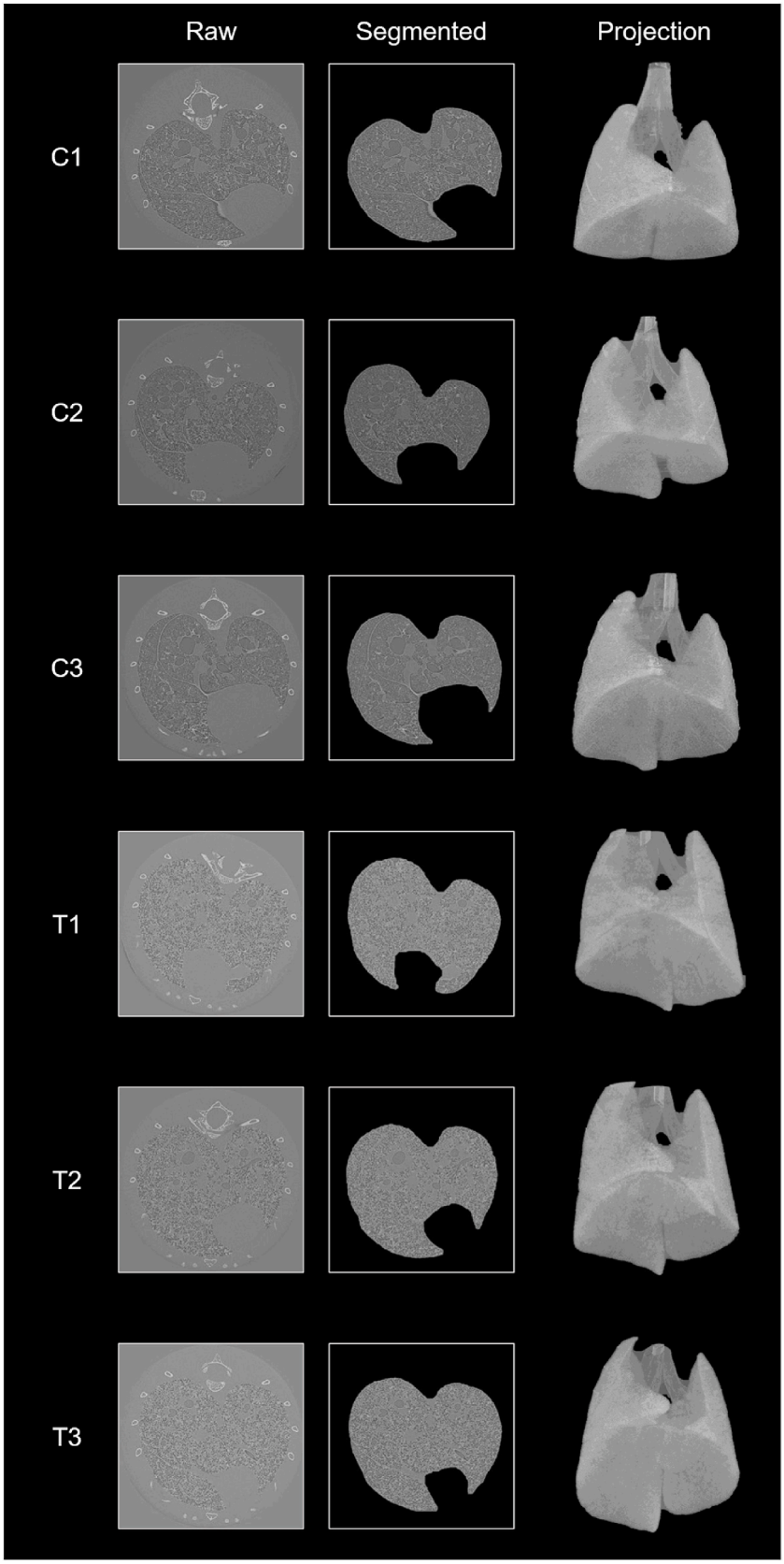

Fig. 2. Raw reference images from samples C1-3 (controls) and T1-3 (alveolar lavage samples), alongside their segmentations and three-dimensional projections at 0 cmH_2O. The length of each edge on the raw and segmented square images is 16.4 mm.

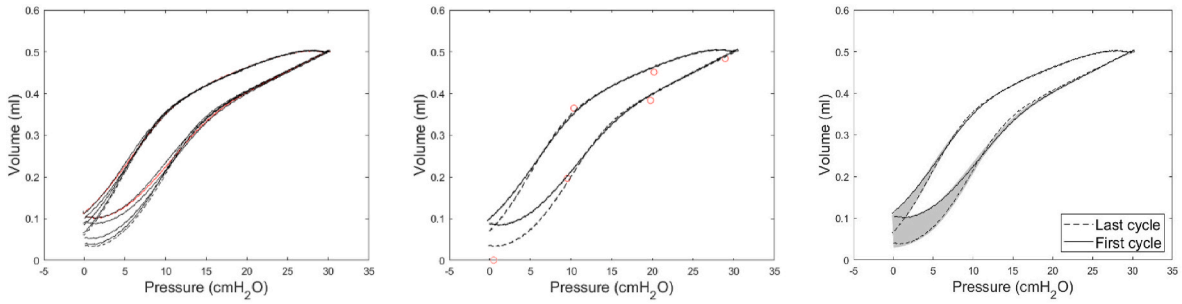

Fig. 3. A characteristic P–V curve for one of the samples focusing on: (left) the repeatability of each cycle and the stability of compliance throughout the experiment; (centre) a comparison of the measured volume changes extracted from the images. Discrete points of volume calculated from the images are overlaid at its corresponding pressure; and (right) a shadow rendering of the repeat cycles highlighting the first and last test cycle.

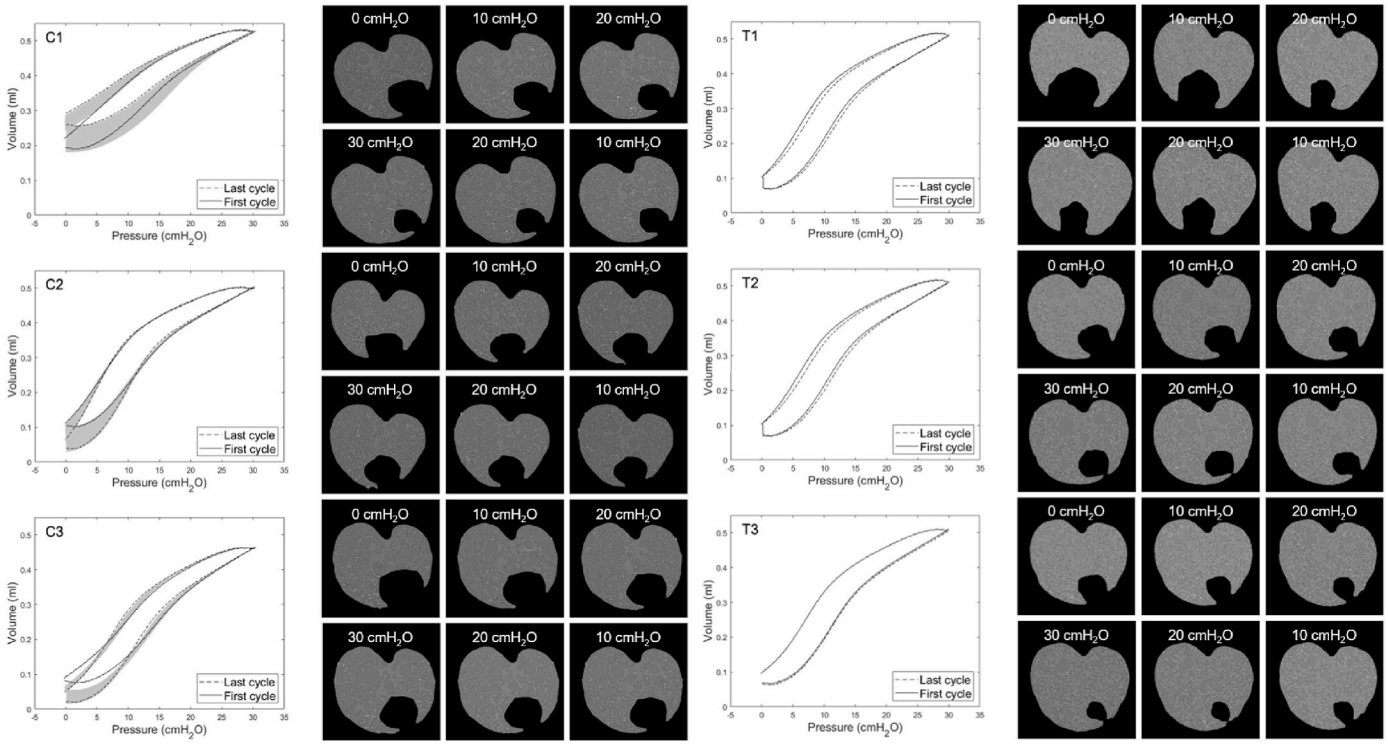

Fig. 4. Lung integrity overview throughout experiment for the control samples (left) and lavage test samples (right). A collation of all P–V curves and their respective segmented images are shown for each sample. The repeatability of each cycle, stability of compliance and consistency of image characteristics throughout the experiment for each sample is highlighted. The length of each edge on the raw and segmented square images is 16.4 mm.

appearance seems fairly consistent, confirming no major changes due to test duration or beam damage, as indicated by the relatively stable and repeatable P–V curves. The apparent difference in C1 compared to the other control samples is revealed in the strain analysis.

Further reinforcement of the experimental procedure can be studied via the quality of the correlation coefficients recorded from the first scans to the last. The majority of each lung volume maintained >95% score throughout with some regions lowering to 90%. Given these samples are highly viscoelastic tissues being imaged, it is an indicator that image clarity (minimized blur) is sufficient to ensure correlations were performed near as well as feasible for these intervals of loading (steps of 10 cmH_2O). Further incremental steps in pressure loading could be added to obtain refined information between phases of loading but the focus here was to ensure minimal risk of radiation interference on the local strain behaviour, particularly when differentiating between controls and lavage test samples.

It is interesting to note from Fig. 5, within the 0 cmH_2O column of strain data, that streaks of higher strain are observed aligning with boundaries separating lung lobes. To produce this 0 cmH_2O dataset the lungs were ventilated then imaged once, and then cycled and imaged again at the same 0 cmH_2O point. The bulk of the volume remains at near zero strain (<0.3%) as desired. Small movements over a period of 5 minutes between scans sees some movement of the large structures with respect to each other. These subtle movements give rise to an apparent 2–10% strain being observed in the joining lines between lobes. However, these recorded strains in the zero-strain test are more of an indicator of macroscale motion within the thoracic cavity as the lung settles in its position rather than deformation of the lung tissue itself. Although an artefact of the DVC computation, which could be avoided through additional masked sub-volumes to some extent, it does highlight the overarching layout of each lung. Moreover, these erroneously recorded larger strains make up a small portion of the total volume. The key indicator is that the bulk tissue demonstrates a low baseline level of strain recorded for this zero-strain test, providing confidence in regional tissue strain analyses during the loading phases at pressures above 0 cmH_2O.

General upward trends in tissue strains are observed for samples T1-3

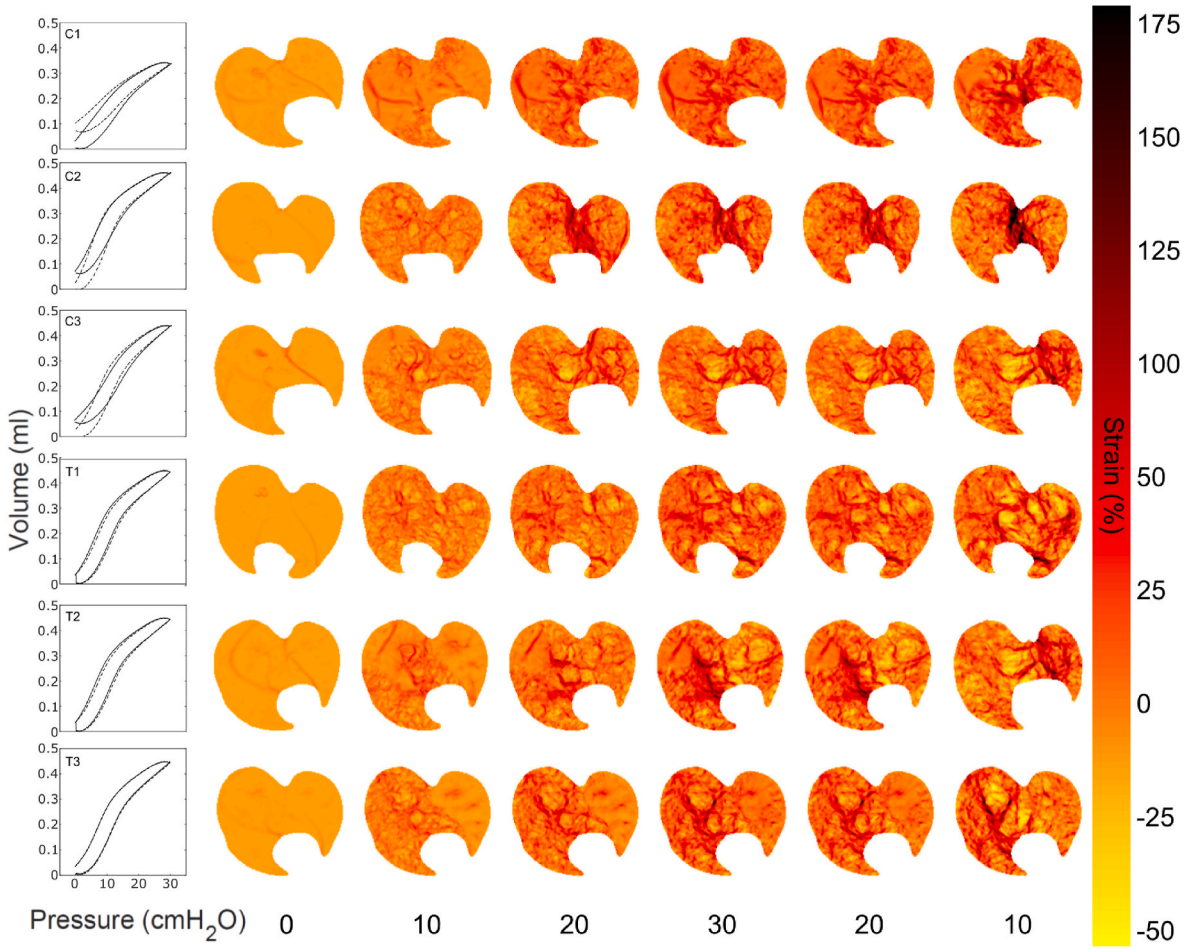

Fig. 5. A lung mechanical overview of each test sample showing the characteristic P–V curve (global measure) and the strain distribution for a sample cross-section of each 3D volume (local measure). Maximum principal 3D strain plots are shown for each pressure interval recorded during an inflation and deflation between 0 and 30 cmH_2O.

during the respiratory cycle when compared to C1-3. There are clear differences in maximum strains observed in localised regions of the parenchyma for samples T1-3 compared to C1-3. Significant volumes of tissue observed upward of 150% strain compared to control samples which showed less than 100% strain across most of each lung volume. The prevalence of highly strained tissue was much more frequent throughout the volumes in the lavage samples, due to this constriction of airways causing redistribution of flow through the easiest path, naturally causing some regions of tissue to take the added burden.

4. Discussion

Studying the raw tomographic images from Fig. 2 further, it is feasible to extract total lung volume change. There are potential questions regarding the volume delivered and volume change within the lung, given a pressure-controlled system is driving the ventilation and the lung is housed within the bounds of the thoracic cavity (finite space of a given chest wall compliance). Fig. 3 highlighted a P–V curve with the calculated volume taken from each segmented image for that test. Here, all the segmented (i.e. non-zero) voxels are added up from each image stack and the differences in volume computed with respect to the zero-pressure stage. This calculated volume change further supports the interpretation of a P–V curve in this context, since the whole lung could be imaged to confirm the global deformation (volume change) are sensible. The remotely controlled ventilator device (CiT), therefore, delivered deformations as desired.

The mean tissue strains in the lavage samples rise significantly compared to samples C1-3. However, there are some interesting details to observe in the strain fields with regards to air trapping and redistribution of tissue strain. Despite numerous ventilation cycles there remained some pathways that were fully or partially occluded, meaning regions of parenchyma downstream remain at relatively low strain. These scenarios of airway blockages can occur in practice and so represent realistic scenarios worth deeper investigation as to their impact on regional tissue strain. All samples except C2 and T1 exhibit some regions, particularly early, on which appear to have trapped air. This gave rise to near bimodal or skewed strain distributions for these lung volumes compared to C2 and T1 which had singly dominant profiles in strain distribution within the bulk tissue.

The value of DVC analysis in showcasing local vs global observations is clear. In C3 for instance, the redistribution of strain once a pathway of ventilation opens is apparent. Focusing on the transition in strain field from 10 cmH_2O to 20 cmH_2O, on the left side of the lung (as it appears in Fig. 5), there is a distinct strain relief observed as the occluded airspace is opened. Having circumstances where regions of airways are being overloaded can lead to redistribution of airflow which overloads other regions of the lung. Even after any blocked pathways are reopened, signs of damage remain visible in the strain patterns. Such strain maps may be used to extend computational methods for inferring material parameters. For example, inverse finite element methods are now using rich strain measurement datasets to generate insight to material properties and structural conditions [51]. Multiscale approaches to image localised tissue strain coupled with computational approaches may help isolate mechanisms in play within complex pathologies (e.g. fluid versus solid

mechanics contributions). Such strain maps can also been used to validate physical surrogate development [52].

Fig. 6 presents the strain distribution overview for control and test samples, comparing C2 and T1 which had minimal signs of air trapping and another pair C1 and T3. Aside from global differences spatially within a given lung, there are trends observed across the different phases of respiration. For instance, both samples will require more pressure to get inflated initially. However, the control samples (with surfactant) can experience an easier and more uniform increase in volume intake earlier. The test sample however shows a more broad distribution due to redistribution of air through paths of least resistance causing regions of higher and lower strains to form across the lung. Studying Fig. 5 for the two samples that have fairly open airways (no obvious signs of blockages), the low-pressure loading produces fairly even strain profiles. At 20 cmH_2O, however, C2 inflates more smoothly, extending its strain distribution with a mean around 75%. T1 displays spikes in its strain distribution, indicative of unstable pathways of variable resistance, and continued broad strain distribution above the bulk of the tissue seen in C2. The airways of C2 fully expand. However, the micromotion of the airways in the ribcage forge a bimodal distribution to appear part way through the test. The bulk of those high strains are apparent to the motion of the upper airways visible in Fig. 5, which smear the control strain data. This artefact in strain calculation occurs around comparatively poor feature contrast regions of the upper airways, given imaging was optimised for capturing the contrast of air and solid. Potential errors for relatively low feature regions of the large airways could be removed by applying a mask and further restraint on the sample head during the test. Further advancements in imaging resolution and speed will also provide opportunities for measurement refinement [33]. However, it is important to demonstrate the interpretation of DVC results and identify mechanisms behind the computed results. The true deformation of interest, lies within the bulk tissue, as this is the area most at risk of potential over pressurisation during ventilation.

The bulk tissue strain of C2 sits in that first part of the distribution, fully expanded, with a mean strain around 75%. For the lavage sample, T1, even at high pressure the bulk of the tissue remains relatively low strains with the frequency of strain spikes increasing throughout the volume. This raise to very high strain gradients, due to redistribution of flow through low-resistance pathways, leads to more significant potential for damage in the bulk tissue. It is important to refer to the regional strain profiles in Fig. 5 as well as these global summaries in strain distribution or P–V to gauge the true nature of deformation in each sample. This observation in local strain gradients is an indicator why prolonged exposure to forced mechanical ventilation always results in a degree of tissue degradation. There will be optimised profiles of loading and pressure parameter bounds to mitigate this level of degradative strain, but this is the trade-off between ventilation (oxygenation) and over-distension (ventilator induced lung injury).

C1 and T3 are two samples which had some degree of air trapping or airway blockages. It is interesting here in Fig. 6 for the bottom traces that C1 has minimal deformation at 10 cmH_2O. There are some clear signs of skewness resulting from this non-ideal loading against blocked pathways. By the 20 cmH_2O loading phase parts of the control sample that had been blocked are opening. This results in C1 showing higher strains approaching the magnitudes of those studied in C2. However, there remains a tail of low strain which is due to some regions remaining blocked causing small spikes in strain in their surrounding pathways to compensate. Despite clearing blockages and redistributing airflow more uniformly, signs remain of the altered deformation profile within the lung. With these pairs of samples it is only at 30 cmH_2O where T3 starts to open up excessively and overshoots again to regions of very high and potentially injurious levels of tissue strain. Such visualisations provide insights towards lung airway management in clinical settings. Many manipulations occur through practiced hands to free blockages early, interpreting global measures of lung health. Here, detailed localised information enables a picture to be painted of lung management under mechanical ventilation. The risks are reinforced regarding potential for ventilator induced lung injury when attempting to maintain and open diseased airways. Having the full lung overview at this resolution will lend itself well to exploring a range of management options and their impact on both the local and global lung performance.

5. Conclusion

Synchrotron radiation micro-CT imaging of murine lungs was successfully performed recording a sequence of images to enable whole organ digital volume correlation (DVC) measurements. Control and alveolar lavage samples were imaged during *in situ* mechanical ventilation. Local and global observations in strain fields helped identify complications in mechanical ventilation. It is clear that even momentary

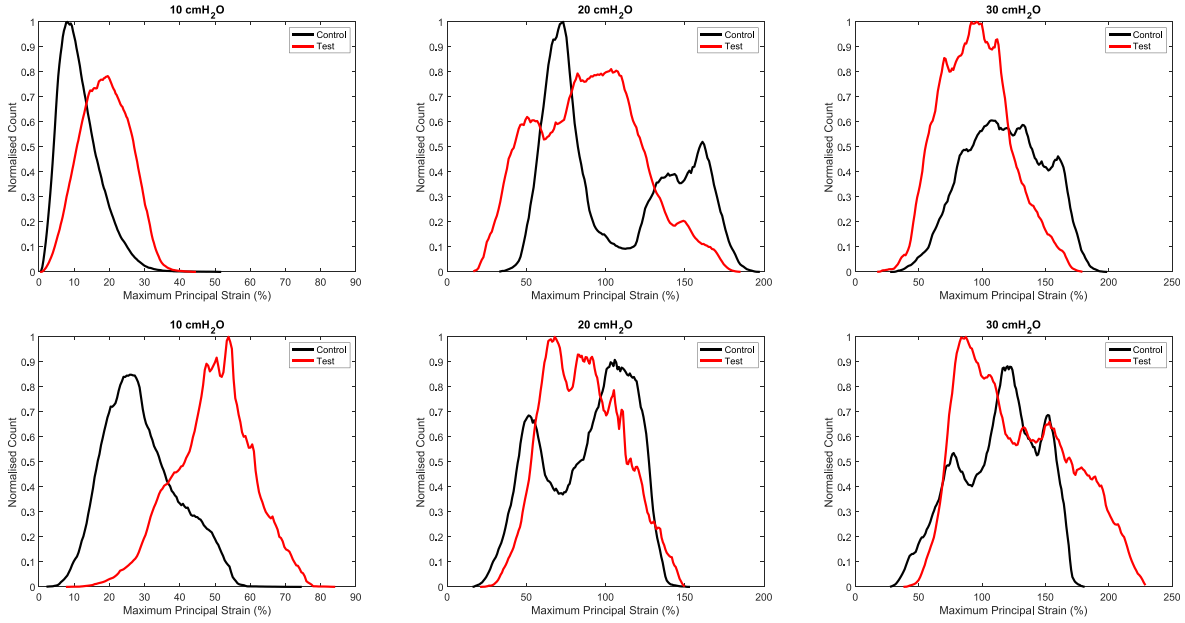

Fig. 6. Normalised strain distributions for the inflation phase from 10 cmH_2O to 30 cmH_2O from left to right for Control and Test samples: (top) C2 and T1; and (bottom) C1 and T3.

loss of airway integrity can lead to excessive redistributions in tissue burden across this delicate organ. This strain redistribution during a mechanical ventilation highlights the multiple pathways for ventilator induced lung injury to occur. It also highlighted the additional complications provided by disease (in the case of a lack of surfactant) giving rise to some very high and injurious deformations. The next phase of work aims to develop efficient links to computational modelling methods to enable distinct mechanisms of lung strain to be identified. Fluid mechanical and solid mechanical contributions to distension plots in the context of ventilation pathways will be important to help discern between effects of different disease types and for individual case by case complications. This dataset will provide very rich validation for a wide range of modelling approaches and this test framework is highly versatile for study across all pathologies.

CRediT authorship contribution statement

Hari Arora: Conceptualization, Data curation, Formal analysis, Funding acquisition, Investigation, Methodology, Project administration, Resources, Visualization, Writing – original draft, Writing – review & editing. **Dale Kernot:** Formal analysis, Software, Visualization, Writing – review & editing, Investigation. **Louis Giron:** Formal analysis, Investigation, Software, Visualization. **David Howells:** Formal analysis, Investigation, Software, Visualization. **Michael Darcy:** Formal analysis, Software, Visualization. **Makoto Hoshino:** Data curation, Formal analysis, Investigation, Methodology, Visualization, Writing – review & editing. **Kentaro Uesugi:** Data curation, Formal analysis, Investigation, Methodology, Visualization, Writing – review & editing. **Raoul van Loon:** Formal analysis, Software, Visualization, Writing – review & editing, Funding acquisition. **Gaku Tanaka:** Conceptualization, Data curation, Formal analysis, Funding acquisition, Investigation, Methodology, Visualization, Writing – review & editing. **Toshihiro Sera:** Conceptualization, Data curation, Formal analysis, Funding acquisition, Investigation, Methodology, Project administration, Resources, Visualization, Writing – original draft, Writing – review & editing.

Declaration of competing interest

The authors declare the following financial interests/personal relationships which may be considered as potential competing interests: Hari Arora reports financial support was provided by The Royal Society. Hari Arora reports financial support was provided by Engineering and Physical Sciences Research Council. Hari Arora reports financial support was provided by Japan Synchrotron Radiation Research Institute. Hari Arora reports a relationship with The British Society for Strain Measurement that includes: board membership. If there are other authors, they declare that they have no known competing financial interests or personal relationships that could have appeared to influence the work reported in this paper.

Data availability

"Data used in this manuscript is very large, e.g. some files >300GB. Therefore selected raw or processed data will be made available upon request within reasonable/practical limits of file sharing."

Acknowledgments

This work was supported by the Royal Society International Exchanges IEC\R3\170065, EPSRC EP/V041789/1. The synchrotron radiation experiments were performed at BL20B2 of SPring-8 with the approval of the Japan Synchrotron Radiation Research Institute (JASRI) (Proposal No.2019A1310).

References

[1] British Lung Foundation, https://statistics.blf.org.uk/(last accessed 29/10/2023).
[2] The World Health Organisation https://www.who.int/health-topics/chronic-respiratory-diseases (last accessed 29/10/2023).
[3] T. Sera, H. Yokota, K. Uesugi, N. Yagi, Airway distension during lung inflation in healthy and allergic-sensitised mice *in vivo*, Respir. Physiol. Neurobiol. 185 (2013) 639–646.
[4] T. Sera, H. Yokota, G. Tanaka, K. Uesugi, N. Yagi, R.C. Schroter, Murine pulmonary acinar mechanics during quasi-static inflation using synchrotron refraction-enhanced computed tomography, J. Appl. Physiol. 115 (2013) 219–228.
[5] H. Arora, A. Nila, K. Vitharana, J.M. Sherwood, T.-T.N. Nguyen, A. Karunaratne, I. K. Mohammed, A.J. Bodey, P.J. Hellyer, D.R. Overby, et al., Microstructural Consequences of blast lung injury characterized with digital volume correlation, Front. Mater. 4 (2017).
[6] L. Broche, P. Pisa, L. Porra, L. Degrugilliers, A. Bravin, M. Pellegrini, J.B. Borges, G. Perchiazzi, A. Larsson, G. Hedenstierna, et al., Individual airway closure characterized *in vivo* by phase-contrast CT imaging in injured rabbit lung, Crit. Care Med. 47 (2019) e774–e781.
[7] D.E. Hurtado, B. Erranz, F. Lillo, M. Sarabia-Vallejos, P. Iturrieta, F. Morales, K. Blaha, T. Medina, F. Diaz, P. Cruces, Progression of regional lung strain and heterogeneity in lung injury: Assessing the evolution under spontaneous breathing and mechanical ventilation, Ann. Intensive Care 10 (2020) 1–10.
[8] M. Palanca, G. Tozzi, L. Cristofolini, M. Viceconti, E. Dall'Ara, Three-dimensional local measurements of bone strain and Displacement: comparison of three digital volume correlation approaches, ASME. J Biomech Eng. July 2015 137 (7) (2015) 071006.
[9] O. Betz, U. Wegst, H. Weide, M. Heethoff, L. Helfen, W.-K. Lee, P. Cloetens, Imaging applications of synchrotron X-ray phase-contrast microtomography in biological morphology and biomaterials science. I. General aspects of the technique and its advantages in the analysis of millimetre-sized arthropod structure, J. Microsc. 227 (2007) 51–71.
[10] Andrew J. Feola, Baptiste Coudrillier, John Mulvihill, Diogo M. Geraldes, Nghia T. Vo, Julie Albon, Richard L. Abel, Brian C. Samuels, C. Ross Ethier, Deformation of the Lamina Cribrosa and optic Nerve due to changes in Cerebrospinal fluid pressure, Invest. Ophthalmol. Vis. Sci. 58 (4) (2017) 2070–2078.
[11] T. Sera, K. Uesugi, N. Yagi, K. Umetani, M. Kobatake, S. Imai, High-resolution visualization of tumours in rabbit lung using refraction contrast X-ray imaging, Eur. J. Radiol. 68 (3) (2008) S54–S57. Supplement.
[12] Development of high-resolution 4D *in vivo*-CT for visualization of cardiac and respiratory deformations of small animals, Toshihiro Sera et al, Phys. Med. Biol. 53 (2008) 4285.
[13] Éric Maire, Philip John Withers, Quantitative X-ray tomography, Int. Mater. Rev. 59 (1) (2014) 1–43.
[14] B.K. Bay, T.S. Smith, D.P. Fyhrie, M. Saad, Digital volume correlation: three-dimensional strain mapping using X-ray tomography, Exp. Mech. 39 (1999) 217–226.
[15] B.K. Bay, Methods and applications of digital volume correlation, J. Strain Anal. Eng. Des. 43 (8) (2008) 745–760.
[16] Jussi-Petteri Suuronen, Bernhard Hesse, Max Langer, Marc Bohner, Julie Villanova, Evaluation of imaging setups for quantitative phase contrast nanoCT of mineralized biomaterials, J. Synchrotron Radiat. 29 (3) (2022) 843–852.
[17] Marta Peña Fernández, A.H. Barber, Gordon William Blunn, Gianluca Tozzi, Optimization of digital volume correlation computation in SR-microCT images of trabecular bone and bone-biomaterial systems, J. Microsc. 272 (3) (2018) p213–p228.
[18] Marta Peña Fernández, Silvia Cipiccia, Enrico Dall'Ara, Andrew J. Bodey, Rachna Parwani, Pani Martino, Gordon W. Blunn, Asa H. Barber, Gianluca Tozzi, Effect of SR-microCT radiation on the mechanical integrity of trabecular bone using *in situ* mechanical testing and digital volume correlation, J. Mech. Behav. Biomed. Mater. 88 (2018) p109–p119.
[19] Marta Peña Fernández, Alexander P. Kao, Roxane Bonithon, David Howells, Andrew J. Bodey, Kazimir Wanelik, Witte Frank, Richard Johnston, Hari Arora, Gianluca Tozzi, Time-resolved *in situ* synchrotron-microCT: 4D deformation of bone and bone analogues using digital volume correlation, Acta Biomater. 131 (2021) p424–p439.
[20] F. Gillard, R. Boardman, M. Mavrogordato, D. Hollis, I. Sinclair, F. Pierron, M. Browne, The application of digital volume correlation (DVC) to study the microstructural behaviour of trabecular bone during compression, J. Mech. Behav. Biomed. Mater. 29 (2014) p480–p499.
[21] P.J. Thurner, P. Wyss, R. Voide, M. Stauber, M. Stampanoni, U. Sennhauser, R. Müller, Time-lapsed investigation of three-dimensional failure and damage accumulation in trabecular bone using synchrotron light, Bone 39 (Issue 2) (2006) 289–299.
[22] K. Madi, K.A. Staines, B.K. Bay, et al., *In situ* characterization of nanoscale strains in loaded whole joints via synchrotron X-ray tomography, Nat. Biomed. Eng. 4 (2020) 343–354.
[23] Marta Peña Fernández, Alexander P. Kao, Witte Frank, Hari Arora, Gianluca Tozzi, Low-cycle full-field residual strains in cortical bone and their influence on tissue fracture evaluated via *in situ* stepwise and continuous X-ray computed tomography, J. Biomech. 113 (2020) 110105.
[24] F. Forsberg, R. Mooser, M. Arnold, E. Hack, P. Wyss, 3D micro-scale deformations of wood in bending: synchrotron radiation μCT data analyzed with digital volume correlation, J. Struct. Biol. 164 (Issue 3) (2008) 255–262.
[25] A. Bhartiya, K. Madi, C.M. Disney, L. Courtois, A. Jupe, F. Zhang, A.J. Bodey, P. Lee, C. Rau, I.K. Robinson, M. Yusuf, Phase-contrast 3D tomography of HeLa

cells grown in PLLA polymer electrospun scaffolds using synchrotron X-rays, J. Synchrotron Radiat. 27 (2020) 158–163.
[26] B. Coudrillier, et al., "Phase-Contrast Micro-Computed Tomography Measurements of the Intraocular Pressure-Induced Deformation of the Porcine Lamina Cribrosa,", in: IEEE Transactions on Medical Imaging, vol. 35, April 2016, pp. 988–999, https://doi.org/10.1109/TMI.2015.2504440, 4.
[27] Effect of tidal volume on distribution of ventilation assessed by synchrotron radiation CT in rabbit, in: L. Porra, S. Monfraix, G. Berruyer, G. Le Duc, C. Nemoz, W. Thomlinson, P. Suortti, A.R.A. Sovijärvi (Eds.), S. Bayat Journal of Applied Physiology 96 (5) (2004) 1899–1908.
[28] T. Sera, K. Uesugi, N. Yagi, Refraction-enhanced tomography of mouse and rabbit lungs, Med. Phys. 32 (2005) 2787–2792.
[29] E. Borisova, G. Lovric, A. Miettinen, et al., Micrometer-resolution X-ray tomographic full-volume reconstruction of an intact post-mortem juvenile rat lung, Histochem. Cell Biol. 155 (2021) 215–226.
[30] Dubsky Stephen, B. Hooper Stuart, Siu Karen K. W. and Fouras Andreas 2012Synchrotron-based dynamic computed tomography of tissue motion for regional lung function measurement, J. R. Soc. Interface (2024) 92213.
[31] H. Arora, R.L. Mitchell, R. Johnston, M. Manolesos, D. Howells, J.M. Sherwood, A. J. Bodey, K. Wanelik, Correlating local Volumetric tissue strains with global lung mechanics measurements, Materials 14 (2021) 439.
[32] G. Lovric, R. Mokso, F. Arcadu, et al., Tomographic *in vivo* microscopy for the study of lung physiology at the alveolar level, Sci. Rep. 7 (2017) 12545.
[33] C.L. Walsh, P. Tafforeau, W.L. Wagner, et al., Imaging intact human organs with local resolution of cellular structures using hierarchical phase-contrast tomography, Nat. Methods 18 (2021) 1532–1541, https://doi.org/10.1038/s41592-021-01317-x.
[34] E. Dall'Ara, A.J. Bodey, H. Isaksson, et al., A practical guide for *in situ* mechanical testing of musculoskeletal tissues using synchrotron tomography, J. Mech. Behav. Biomed. Mater. 133 (2022) 105297.
[35] H. Chu, J.F.W. Chan, K.Y. Yuen, Animal models in SARS-CoV-2 research, Nat. Methods 19 (2022) 392–394, https://doi.org/10.1038/s41592-022-01447-w.
[36] Z. He, F. Ye, C. Zhang, J. Fan, Z. Du, W. Zhao, Q. Yuan, W. Niu, F. Gao, B. He, P. Cao, L. Zhao, X. Gao, X. Gao, B. Sun, Y. Dong, J. Zhao, J. Qi, X.J. Liang, H. Jiang, Y. Gong, W. Tan, X. Gao, A comparison of Remdesivir versus gold cluster in COVID-19 animal model: a better therapeutic outcome of gold cluster, Nano Today 44 (2022 Jun) 101468, https://doi.org/10.1016/j.nantod.2022.101468.
[37] G. Zhang, Y. Cong, F.L. Liu, et al., A nanomaterial targeting the spike protein captures SARS-CoV-2 variants and promotes viral elimination, Nat. Nanotechnol. 17 (2022) 993–1003, https://doi.org/10.1038/s41565-022-01177-2.
[38] T. Eftaxiopoulou, et al., Prolonged but not short-duration blast waves elicit acute inflammation in a rodent model of primary blast limb trauma, Injury 47 (Issue 3) (2016) 625–632.
[39] A. Barnett-Vanes, et al., CD43Lo classical monocytes participate in the cellular immune response to isolated primary blast lung injury, J. Trauma Acute Care Surg. 81 (3) (2016) 500–511.
[40] Ludovic Broche, Gaetano Perchiazzi, Liisa Porra, Angela Tannoia, Mariangela Pellegrini, Savino Derosa, Alessandra Sindaco, João Batista Borges, Loïc Degrugilliers, Anders Larsson, Göran Hedenstierna, Anthony S. Wexler, Alberto Bravin, Sylvia Verbanck, Bradford J. Smith, Jason H.T. Bates, Sam Bayat, Dynamic mechanical Interactions between neighboring airspaces determine cyclic opening and closure in injured lung, Crit. Care Med. 45 (4) (2017) 687–694.
[41] H.D. Litzlbauer, K. Korbel, T.L. Kline, S.M. Jorgensen, D.R. Eaker, R.M. Bohle, E. L. Ritman, A.C. Langheinrich, Synchrotron-based micro-CT imaging of the human lung acinus, Anat. Rec. 293 (2010) 1607–1614.
[42] S. Schleede, et al., Emphysema diagnosis using X-ray dark-field imaging at a laser-driven compact synchrotron light source, Proc. Natl. Acad. Sci. USA 109 (44) (2012), 17880–17885.
[43] Stephen Milne, Gregory G. King, Advanced imaging in COPD: insights into pulmonary pathophysiology, J. Thorac. Dis. 6 (2014) 11. November 18, 2014): Journal of Thoracic Disease (Chronic Obstructive Pulmonary Disease) 2014.
[44] L. Porra, L. Dégrugilliers, L. Broche, et al., Quantitative imaging of regional aerosol deposition, lung ventilation and morphology by synchrotron radiation CT, Sci. Rep. 8 (2018) 3519.
[45] E. Dall'Ara, M. Peña-Fernández, M. Palanca, M. Giorgi, L. Cristofolini, G. Tozzi, (3 more authors) precision of digital volume correlation approaches for strain analysis in bone imaged with micro-computed tomography at different dimensional levels, Front. Mater. 4 (2017) 31.
[46] S. Tavana, J. Clark, J. Prior, N. Baxan, S. Masouros, N. Newell, U. Hansen, Quantifying deformations and strains in human intervertebral discs using Digital Volume Correlation combined with MRI (DVC-MRI), J. Biomech. 102 (2020) 109604.
[47] S.V.A. Acosta, G.M. Flechas, J. Molimard, S. Avril, Three-dimensional full-field strain measurements across a whole porcine aorta subjected to tensile loading using optical coherence tomography–digital volume correlation, Front. Mech. Eng. 4 (2018) 3.
[48] A. Levchuk, P. Schneider, M. Meier, P. Vogel, F. Donaldson, R. Müller, An automated step-wise micro-compression device for 3D dynamic image-guided failure assessment of bone tissue on a microstructural level using time-lapsed tomography, Front. Mater. 5 (2018) 32.
[49] C. Franck, S. Hong, S.A. Maskarinec, et al., Three-dimensional full-field measurements of large deformations in soft materials using confocal microscopy and digital volume correlation, Exp. Mech. 47 (2007) 427–438, https://doi.org/10.1007/s11340-007-9037-9.
[50] S. Goto, K. Takeshita, Y. Suzuki, H. Ohashi, Y. Asano, H. Kimura, T. Matsushita, N. Yagi, M. Isshiki, H. Yamazaki, Y. Yoneda, K. Umetani, T. Ishikawa, Construction and commissioning of a 215-m-long beamline at SPring-8, Nucl. Instrum. Methods Phys. Res. Sect. A Accel. Spectrom. Detect. Assoc. Equip. 467–468 (2001) p682–p685. Part 1.
[51] M. Maghsoudi-Ganjeh, C. Mariano, S. Sattari, H. Arora, M. Eskandari, Developing a lung model in the age of COVID-19: a digital image correlation and inverse finite element analysis framework, Front. Bioeng. Biotechnol. 9 (2021).
[52] Olivier Ranunkel, Firat Güder, Hari Arora, ACS Appl. Bio Mater. 2 (4) (2019) 1490–1497.